Multiline Assessment of Narrow-line Regions in z similar to 3 Radio Galaxies

The Astrophysical Journal, 929:51 (15pp), 2022 April 10 https://doi.org/10.3847/1538-4357/ac5b71

Multiline Assessment of Narrow-line Regions in $z \sim 3$ Radio Galaxies

Koki Terao[1], Tohru Nagao[2], Kyoko Onishi[2,3], Kenta Matsuoka[4], Masayuki Akiyama[1], Yoshiki Matsuoka[2], and Takuji Yamashita[2,5]

[1] Astronomical Institute, Tohoku University, Aramaki, Aoba-ku, Sendai, Miyagi 980-8578, Japan
[2] Research Center for Space and Cosmic Evolution, Ehime University, Bunkyo-cho 2-5, Matsuyama, Ehime 790-8577, Japan
[3] Department of Space, Earth and Environment, Chalmers University of Technology, Onsala Space Observatory, SE-439 92 Onsala, Sweden
[4] Utena Meishu Company, Limited, 519-1 Morimatsu-machi, Matsuyama, Ehime 791-1113, Japan
[5] National Astronomical Observatory of Japan, 2-21-1 Osawa, Mitaka, Tokyo 181-8588, Japan
Received 2021 September 6; revised 2022 February 22; accepted 2022 March 5; published 2022 April 12

Abstract

In this paper, we use high-quality rest-UV spectra of three radio galaxies at $z \sim 3$ observed with the FORS2 camera on the Very Large Telescope to measure the flux of several emission lines, including relatively faint ones, such as N IV]λ1486, O III]λ1663, and [Ne IV]λ2424. Additionally, we collect fluxes of faint rest-UV emission lines in 12 $z \sim 3$ radio galaxies from the literature. Previously, physical and chemical properties of narrow-line regions (NLRs) in high-z active galactic nuclei (AGNs) have been investigated mostly by using only strong rest-UV emission lines (e.g., N Vλ1240, C IVλ1549, He IIλ1640, and C III]λ1909). Such strong-line diagnostics are based on various assumptions due to the limitation in the number of available emission-line constraints. In this work, both physical and chemical properties of NLR clouds in each object are estimated by fitting detailed photoionization models to the measured emission-line fluxes. We confirm that the metallicity of NLRs in AGNs at $z \sim 3$ is solar or supersolar, without assumptions about the gas density and ionization parameter thanks to the constraints from the faint emission lines. This result suggests that high-z radio galaxies are already chemically mature at $z \sim 3$.

Unified Astronomy Thesaurus concepts: Active galaxies (17); Interstellar medium (847); Active galactic nuclei (16)

1. Introduction

Understanding the formation and evolution of galaxies is one of the hot topics in modern astronomy. To tackle this topic, investigating the nature of galaxy components such as stars, gas, and dark matter at various cosmic epochs is a fundamental approach. It is especially important to understand the redshift evolution of interstellar medium (ISM) properties that are characterized by physical and chemical parameters such as gas density, ionization parameter, and metallicity. In particular, metallicity reflects the star formation and gas inflow/outflow history of galaxies (e.g., Erb 2008; Lilly et al. 2013; Lu et al. 2015; Belfiore et al. 2016; Vangioni et al. 2018). ISM properties in low-redshift galaxies are usually estimated with optical emission-line diagnostics (e.g., Nagao et al. 2006a; Izotov et al. 2006; Kewley & Ellison 2008; Curti et al. 2017, 2020). For galaxies at high redshifts ($z > 1$), the rest-frame optical emission lines are shifted into the near-infrared, and thus measurements of their strength are more challenging. Recently, the ISM properties of such high-z star-forming galaxies have been also investigated (e.g., Förster Schreiber et al. 2009; Yabe et al. 2012; Yuan et al. 2013; Maier et al. 2014; Newman et al. 2014; Nakajima et al. 2018; Sanders et al. 2020), and the observed evolution of the emission-line properties is consistently explained with photoionization models with extreme ISM conditions (e.g., Kewley et al. 2013). However, the determination of detailed physical parameters of the ISM for high-z star-forming galaxies is generally difficult because their emission lines are faint.

On the other hand, active galactic nuclei (AGNs) are luminous, and thus their emission-line fluxes can be measured even in the high-z universe. One important advantage of the spectroscopic study of AGNs in comparison to that of star-forming galaxies is that AGNs show strong rest-frame UV emission lines, which are faint in star-forming galaxies. Many spectroscopic observations for high-z AGNs have been carried out for various diagnostic studies (e.g., Villar-Martín et al. 1999; De Breuck et al. 2000; Vernet et al. 2001; Solórzano-Iñarrea et al. 2004; Nagao et al. 2006b; Humphrey et al. 2008; Matsuoka et al. 2011a; Feltre et al. 2016). Particularly, spectroscopic properties of narrow-line regions (NLRs) in AGNs have been often investigated because NLR gas clouds distribute up to the kiloparsec scale, which can trace a far larger scale than broad-line regions (BLRs; located at $\lesssim$1 pc typically), and thus the NLR is more appropriate for studying the ISM property of AGN host galaxies. Since NLR clouds are mostly ionized through the photoionization process (e.g., Binette et al. 1996; Komossa & Schulz 1997; Groves et al. 2004; Thomas et al. 2016), the ISM properties of host galaxies can be studied through detailed comparisons between photoionization models and emission-line spectra of NLRs.

To study the spectroscopic properties of NLRs in AGNs, more reliable measurements of the emission-line properties of the NLRs can be obtained for Type 2 AGNs than for Type 1 AGNs. This is because the strong broadline emission from BLRs in Type 2 AGNs is blocked by optically thick dusty tori, and thus both of forbidden and permitted emission lines can be used for various diagnostic studies without being affected by the BLR emission, which only appears in the permitted

emission lines. Among some populations of Type 2 AGNs, high-z radio galaxies (HzRGs) have often been targeted in high-z spectroscopic studies because they are easier to be found than radio-quiet ones. In previous spectroscopic studies of HzRGs, strong UV lines (e.g., N Vλ1240, C IVλ1549, He IIλ1640, and C III]λ1909) have been used to characterize their ISM properties (e.g., Nagao et al. 2006b; Villar-Martín et al. 2007; Humphrey et al. 2008; Matsuoka et al. 2009; Dors et al. 2014; Morais et al. 2017; Matsuoka et al. 2018). The results of these studies suggest that the HzRGs were already chemically mature by $z \sim 4$, and no significant redshift evolution in $1 < z < 4$ is observed.

In the previous studies, however, emission-line diagnostic studies have required assumptions on some ISM parameters; in other words, it has been difficult to determine the physical and chemical parameters of the ISM simultaneously due to the small number of detected emission lines. For example, the gas metallicity has sometimes been estimated with C IV/He II and C III]/C IV flux ratios assuming a fixed gas density (e.g., Matsuoka et al. 2009). The C IV/He II flux ratio, however, depends on the gas density of ionizing clouds. This flux ratio can vary by ∼2 dex when log n (in cm^{-3}) changes from ∼2 to ∼6 (Matsuoka et al. 2009). Consequently, the results of the metallicity estimations that do not take into account the dependence of these flux ratios on gas density can vary by factor 2 depending on the assumed gas density (e.g., Matsuoka et al. 2018). However, such degeneracies can be solved by using not only traditionally used strong emission lines (Silva et al. 2018), but also faint emission lines. Therefore, in this paper, we use high signal-to-noise (S/N) rest-UV spectra of HzRGs to measure the flux of several emission lines, including relatively weak ones. We investigate the physical and chemical properties of the ISM in HzRGs without assumptions about the gas density and ionization parameter.

This paper is structured as follows. In Section 2 we describe the spectroscopic data and reduction processes. We show the results of the data analysis in Section 3 and describe our photoionization models in Section 4. We discuss the interpretation of our results in Section 5 and draw the conclusion of this paper in Section 6. Throughout this paper, we assume $\Omega_M = 0.3$, $\Omega_\Lambda = 0.7$, and $H_0 = 70$ km s^{-1} Mpc^{-1}.

2. Data

2.1. Our Targets and Data Reduction

To analyze narrow emission lines including faint ones, we investigate the high-quality rest-frame UV spectra of HzRGs presented by Matsuoka et al. (2009). Among the nine HzRGs studied by Matsuoka et al. (2009), we specifically focus on three HzRGs (TN J0920−0712, 4C 24.28, and USS 1545−234) whose high S/N spectra show at least six emission lines with S/N > 5. Thanks to the high S/N, we detect N IV]λ1486, O III]λ1663, and [Ne IV]λ2424 emission lines, which are weaker than the C IV, He II, and C III] emission lines. HzRGs in Matsuoka et al. (2009) were originally selected from a HzRG catalog (De Breuck et al. 2000) with the following criteria: (1) redshift higher than 2.7, and (2) the emission-line flux of C IV, He II, and C III] had not been measured. The basic properties of the three objects are summarized in Table 1. The observations were carried out using the FOcal Reducer and low dispersion Spectrograph 2 (FORS2; Appenzeller et al. 1998) at the Very Large Telescope (VLT) between 2005 October and 2006 October (PI: Tohru Nagao). The slit width was 1″. The spectral resolution was $R \sim 500$, which was measured using the width of sky emission lines. The typical seeing during the observations was ∼1.″4, which is broader than the slit width. The details of the observations are described in Matsuoka et al. (2009).

Table 1
Target Properties

Name	z[a]	$E(B-V)$[b]	Exp. (min)	Date of Observations
TN J0920−0712	2.758	0.041	180	2006 Apr. 3, 4
4C 24.28	2.913	0.018	180	2006 Apr. 23
USS 1545−234	2.751	0.257	240	2006 Apr. 5, 23, 24

Notes.
[a] Redshifts are determined from the observed C IV wavelength.
[b] Galactic extinction (Schlegel et al. 1998).

In this work, we are specifically interested in relatively faint emission lines of the spectra in order to increase available emission lines for estimating ISM parameters. However, Matsuoka et al. (2009) did not correct for the effect of the atmospheric absorption because they focused only on strong emission lines whose wavelengths were not affected by the atmospheric absorption. Thus we reanalyzed the spectra with an additional procedure to correct for the atmospheric absorption, which is not negligible for faint emission lines. The data reduction of the three HzRGs is briefly described below, which is basically the same as described in Matsuoka et al. (2009), except for some additional procedures. The data analysis was performed with the IRAF software (Tody 1986, 1993). We adopt the usual manner to analyze the data, i.e., bias subtraction using average bias frames, flat-fielding, cosmic-ray subtraction, wavelength calibration using sky emission lines, sky subtraction, spectral extraction from two-dimensional spectra by adopting an aperture of 2.″25 (9 pixels), and flux calibration by standard stars. The Galactic reddening maps from Schlegel et al. (1998) and the extinction law from Cardelli et al. (1989) were adopted for the correction of the Galactic reddening of the three targets. Sky subtractions were performed using an averaged sky spectrum created based on the region that is free from the target light in the observed 2D spectrum. Cosmic-ray events were removed using the `lacos_spec` task (van Dokkum 2001) instead of the `fixpix` task used in Matsuoka et al. (2009). The spectra of targets were divided by the reduced spectra of standard stars to correct for atmospheric absorption features, which were not corrected for in the previous analysis.

In general, emission lines from NLRs in AGNs are affected by the internal dust reddening caused in their host galaxies, not only in our galaxy (e.g., Ho et al. 2003; Gu et al. 2006; Vaona et al. 2012; Heard & Gaskell 2016; Malkan et al. 2017; Lu et al. 2019). In order to correct for the internal reddening, the Balmer decrement (Hα/Hβ flux ratio) is usually evaluated. However, it is not easy to estimate the amount of the internal reddening for HzRGs in our sample because Balmer lines shift into the near-infrared wavelength, which was not measured for our sample. In this work, we did not correct for this internal extinction based on the following consideration. For low-redshift radio galaxies, Robinson et al. (1987) investigated the Balmer decrement of 11 radio galaxies at $z < 0.1$ and showed that

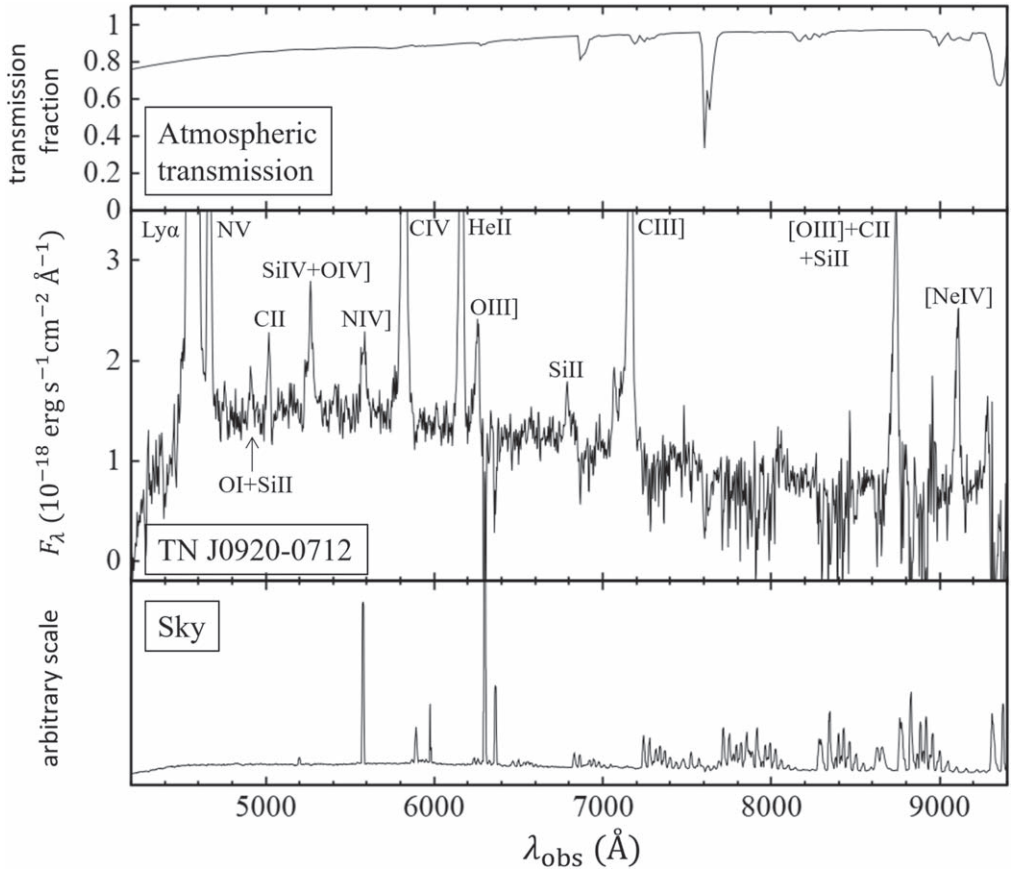

Figure 1. Rest-frame UV spectrum of TN J0920−0712 (middle panel). The detected emission lines are labeled. The top panel shows a typical atmospheric transmission at the VLT site (Noll et al. 2012; Jones et al. 2013). The bottom panel shows a typical sky spectrum obtained during our runs.

extended emission-line regions of more than half of their targets show a flux ratio consistent with case B, thus their internal dust reddening is negligible. For HzRGs at $1.4 < z < 2.6$, Humphrey et al. (2008) investigated flux ratios of Hα/Hβ and/or He IIλ1640/He IIλ4686 of 11 HzRGs and reported that more than half of them showed low extinction ($A_V < 0.5$ mag). Therefore, we assume that the internal dust extinction is negligible for our HzRG sample. We evaluate how extinction correction could affect our results in Section 5.1.

2.2. Additional Rest-UV Data from the Literature

In addition to the reanalyzed data described in Section 2.1, we collect rest-UV emission-line fluxes of 12 HzRGs that show various rest-UV emission lines thanks to high S/N spectra, including relatively weak ones such as N IV]λ1486, O III] λ1663, and [Ne IV]λ2424. The emission-line data of 10 $z \sim 3$ HzRGs were obtained from Vernet et al. (2001) and Humphrey et al. (2008). These targets were selected from the ultra-steep spectrum (USS) radio galaxy survey (Rottgering et al. 1995) for $z > 2.2$ and $R \sim 21$–23 mag. These spectra were observed with the spectro-polarimetric mode of the Low-Resolution Imaging Spectrometer (LRISp; Goodrich et al. 1995; Oke et al. 1995) on the Keck II telescope. Another spectrum of a $z \sim 2$ HzRG (NVSS J002402−325253) obtained with the FORS1 on the VLT is collected from De Breuck et al. (2006). This target had been selected from the USS radio galaxy sample (De Breuck et al. 2004). The other spectrum is 3C 256 ($z = 1.824$), which was observed with the double spectrograph (Oke & Gunn 1982) on the Hale telescope (Simpson et al. 1999).

3. Results

3.1. Rest-frame UV Spectra of the Three HzRGs

The newly reduced spectra of the three objects described in Section 2.1 are shown in Figures 1–3. In these figures, we also show typical atmospheric transmission and a typical sky spectrum.[6] As shown in the figures, there are weak absorption lines and air-grow emission lines around the detected weak emission lines, while these effects are properly corrected. From the spectra, 13 emission lines were detected with S/N > 3 in TN J0920−0712. The spectra of 4C 24.28 and USS 1545–234 show 10 and 9 emission lines, respectively (Table 2).

The fluxes, central wavelengths, FWHMs, and observed equivalent widths (EWs) of the detected emission lines with S/N > 3 were measured with the IRAF task `splot` assuming a single Gaussian profile. Here the flux errors given in Table 2 include the uncertainty due to the pixel-to-pixel variance and the estimation of the continuum level. Note that narrow emission lines in AGN spectra have sometimes been fitted with more sophisticated methods such as a multicomponent Gaussian profile (e.g., Veilleux 1991; Greene & Ho 2005; Mullaney et al. 2013). However, such profiles require a larger number of free parameters than the single Gaussian profile. Since the strength of the weak emission lines can be described by a single Gaussian profile, we adopt a single Gaussian

[6] This sky spectrum was obtained from the SkyCalc sky model calculator (Noll et al. 2012; Jones et al. 2013) provided by ESO (https://www.eso.org/observing/etc/bin/gen/form?INS.MODE=swspectr+INS.NAME=SKYCALC).

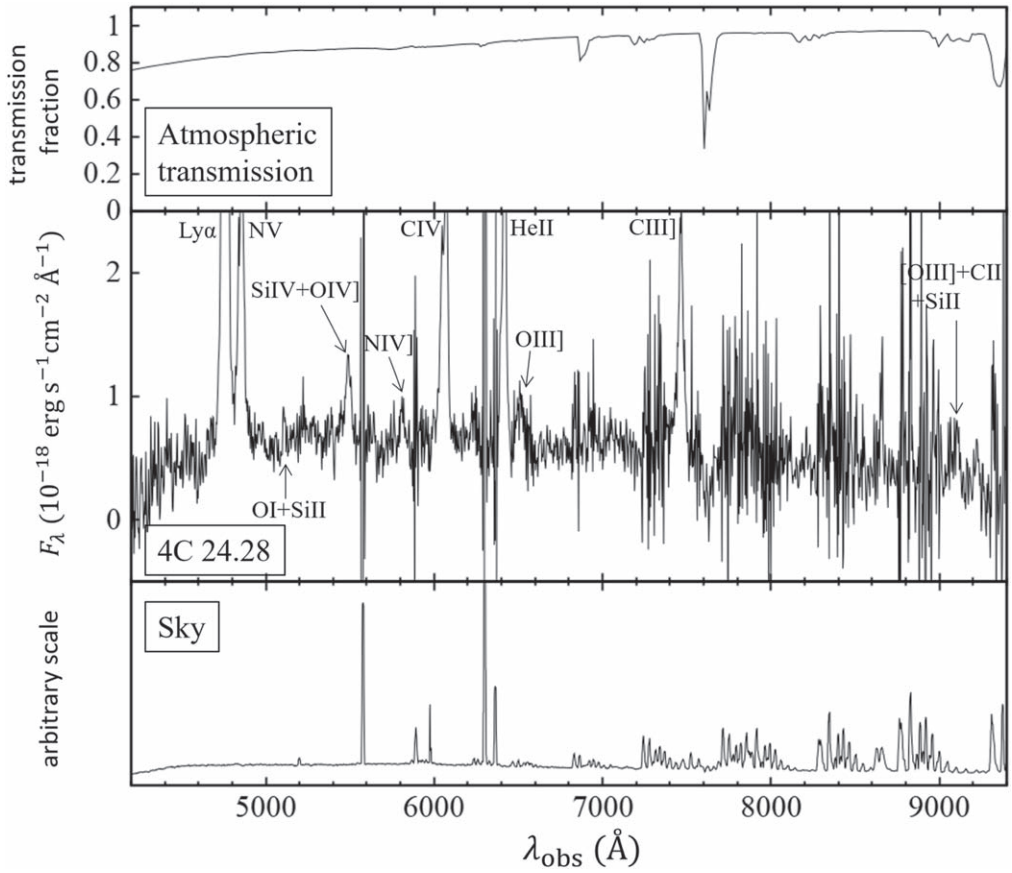

Figure 2. Same as Figure 1, but for 4C 24.28.

profile. The emission-line properties obtained through the fit are given in Table 2. To confirm the consistency between the emission-line fluxes given in Matsuoka et al. (2009) and our results, we compare the emission-line flux ratios obtained in this work and in Matsuoka et al. (2009). The C III]/C IV flux ratio of TN J0920−0712 is 0.615 ± 0.030 in this work and 0.578 ± 0.018 in Matsuoka et al. (2009), thus these values are consistent within the 1σ error range. The remaining two objects also show consistent emission-line flux ratios with Matsuoka et al. (2009); the C III]/C IV flux ratio of 4C 24.28 is 0.657 ± 0.035 in Matsuoka et al. (2009) and 0.719 ± 0.056 in this work, and that of USS 1545−234 is 0.451 ± 0.024 in Matsuoka et al. (2009) and 0.426 ± 0.036 in this work.

3.2. Rest-frame UV Spectra of Additional Data

The compiled fluxes of rest-frame UV emission lines of HzRGs described in Section 2.2 are listed in Table 3. The UV spectrum of $0828 + 193$ shows the largest number of emission lines in our sample (for details, see Table 4 in Humphrey et al. 2008). By combining the emission-line flux ratios of our own sample (Section 3.1) and also the objects taken from the literature (Section 3.2), we discuss the physical and chemical properties of NLRs in HzRGs combined with photoionization models whose details are explained in the next section.

4. Photoionization Model Fitting and Results

4.1. Method

As mentioned in Section 1, the main ionization mechanism of NLR clouds in AGNs has been thought to be the photoionization by ionizing photons from the central engine of AGNs (e.g., Binette et al. 1996; Komossa & Schulz 1997; Groves et al. 2004; Thomas et al. 2016). On the other hand, the collisional ionization of NLR clouds by fast shocks associated with radio jets and outflows has also been suggested for some AGNs (e.g., Knop et al. 1996; Bicknell et al. 1998; Allen et al. 2008; Shih et al. 2013; Terao et al. 2016). Matsuoka et al. (2009) reported that most gas clouds (especially clouds emitting high-ionization emission lines, see Table 4) in NLRs of HzRGs are photoionized, based on a C III]/C IV versus C IV/He II diagnostic diagram (see also Nagao et al. 2006b). Therefore, in this work, physical and chemical properties of ionized gas clouds in NLRs are investigated through the comparison between photoionization models and observed emission-line spectra.

We calculated the flux ratio based on a photoionization model using Cloudy version 13.03 (Ferland et al. 2013). We used the `table AGN` command as the input SED, which reproduces the typical ionizing SED of AGNs (Mathews & Ferland 1987). The parameter ranges covered in the model calculations were the hydrogen gas density $\log n = 2.0-6.0$, the ionization parameter $\log U = -3.0--0.5$, and the metallicity $Z = 0.1-5.0\, Z_\odot$. The step of calculations was 0.1 dex for each parameter, and thus 53,300 models were calculated. The adopted ranges of these parameters are typical for NLRs adopted in the literature (e.g., Nagao et al. 2006b; Feltre et al. 2016). The relative elemental abundance ratio is assumed to be the solar composition (Grevesse et al. 2010), except for helium and nitrogen. For helium, we take the primordial component and the primary nucleosynthesis component into account.

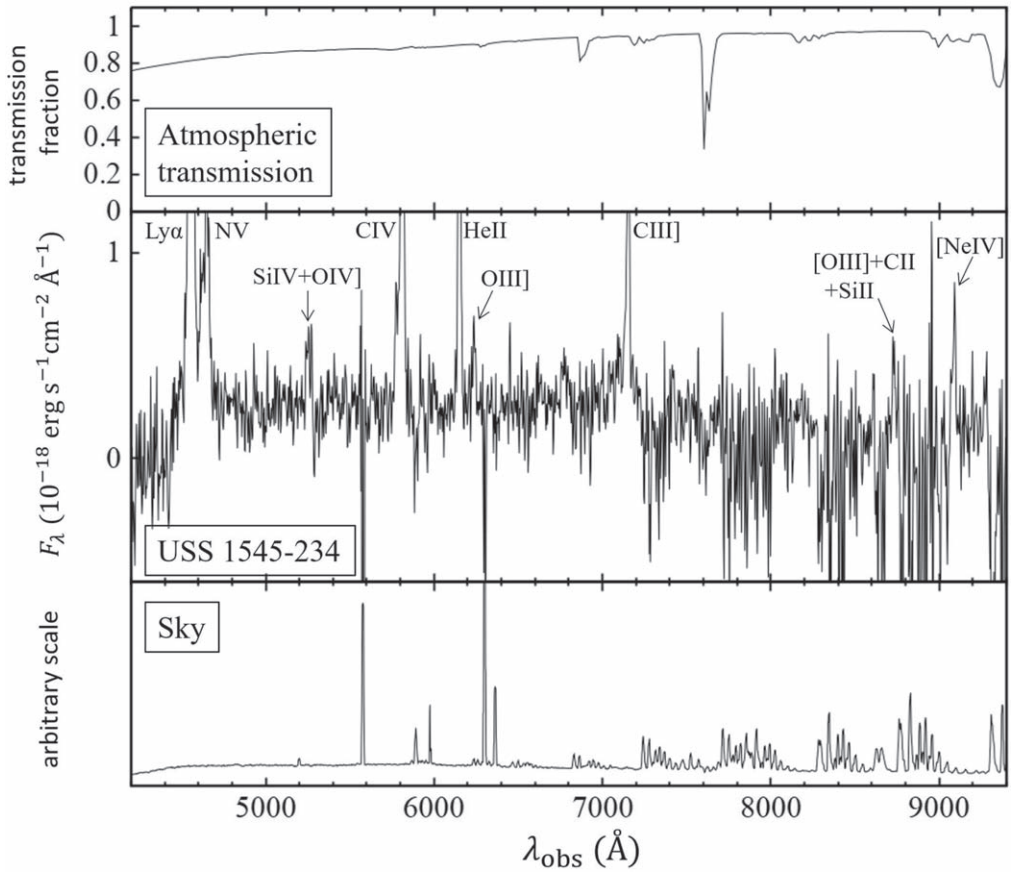

Figure 3. Same as Figure 1, but for USS 1545−234.

Specifically, it is determined by $\mathrm{He/H} = 0.08096 + 0.02618(Z/Z_{\odot})$. The nitrogen relative abundance is assumed to be proportional to the square of the metallicity at the high-metallicity range, taking the nature of nitrogen as a secondary element into account. More specifically, the nitrogen relative elemental abundance is determined by $\log(\mathrm{N/H} = -4.57 + \log(Z/Z_{\odot})$ for 0.1 and $0.2\,Z_{\odot}$ models and $\log(\mathrm{N/H}) = -4.17 + 2\log(Z/Z_{\odot})$ for $Z \geqslant 0.3\ Z_{\odot}$ models. These analytic expressions adopted in this work for helium and nitrogen were taken from Dopita et al. (2000). We assumed dust-free gas clouds in our Cloudy runs, i.e., the relative elemental abundance of gas clouds is without dust depletion. This is because high-ionization lines arise mostly in the inner part of the NLR, where dust grains do not survive (Marconi et al. 1994; Nagao et al. 2003, 2006b). The model calculations were terminated when the ionized fraction of hydrogen dropped to 15% because below this, the gas does not significantly emit rest-frame UV emission lines.

Although the model runs in this work were executed by assuming one-zone constant-density clouds, it has been reported that high-ionization lines and low-ionization lines arise from different parts in the NLR with a significantly different gas density (e.g., Ferguson et al. 1997; Nagao et al. 2001a; Rose et al. 2015; Adhikari et al. 2016). In this work, we focus only on high-ionization lines (Si IV, O IV], N IV], C IV, He II, O III], C III], and [Ne IV]), which are expected to arise from a similar part within NLRs (Table 4). Therefore it is expected that our one-zone treatment does not introduce significant uncertainty.

4.2. Model Results

We determine the model parameters (the gas density, ionization parameter, and gas metallicity) simultaneously by a χ square (χ^2) fitting where the reduced χ^2 ($\tilde{\chi}^2$) is calculated. All line fluxes are normalized by the He II flux, because He II is a recombination line and thus its flux is almost proportional to the number of the He^+-ionizing photons without significant dependences on ISM properties such as the gas density and ionization parameter. Note that although the relative He^+-ionizing photon luminosity depends on the spectral energy distribution (SED), the UV SEDs of AGNs are similar to each other if the Eddington ratio is moderately high, $\gtrsim$0.01 (e.g., Zheng et al. 1997; Koratkar & Blaes 1999; Richards et al. 2006).

Here it should be noted that the error of observed emission-line fluxes given in Table 2 does not include the systematic error of the flux measurements. Indeed, the S/Ns of the strong emission lines are higher than that of faint emission lines. In other words, the weight of faint emission lines is small in the χ^2 fitting. Then, the following systematic errors are considered to exist, and the weight of the strong emission lines is reduced by adding these systematic errors to the error of the observed emission-line fluxes. The FORS2 Absolute Photometry Project reported that the photometric accuracy of the 1σ systematic error is $\sim$2% under photometric conditions.[7] In general, the absolute photometric accuracy of long-slit spectroscopic observations becomes worse than that of photometric

[7] VLT-TRE-ESO-13112-5727 (https://www.eso.org/sci/facilities/paranal/instruments/fors/doc/VLT-TRE-ESO-13112-5727.pdf).

Table 2
Detected Emission Lines

Name	Line	Flux (10^{-17} erg s^{-1} cm^{-2})	λ_{obs}[a] (Å)	FWHM$_{obs}$[b] (Å)	FWHM$_{corr}$[c] (km s^{-1})	EW$_{obs}$ (Å)
TN J0920−0712	Ly$\alpha\lambda$1216	305 ± 1	4568.34 ± 0.01	30.09 ± 0.05	1881 ± 3	3179 ± 341
	N vλ1240	7.14 ± 0.51	4664.63 ± 0.13	26.91 ± 0.83	1662 ± 57	36.88 ± 3.81
	O i+Si iiλ1305	1.15 ± 0.17	4912.57 ± 0.91	31.46 ± 5.20	1821 ± 332	11.18 ± 1.37
	C iiλ1335	1.62 ± 0.16	5017.76 ± 0.29	19.56 ± 1.44	1001 ± 101	12.80 ± 1.87
	Si ivλ1397+O iv]λ1402	4.24 ± 0.41	5265.02 ± 0.17	38.32 ± 1.13	2098 ± 67	26.52 ± 1.24
	N iv]λ1486	2.50 ± 0.19	5581.59 ± 0.10	37.68 ± 0.94	1933 ± 53	19.85 ± 0.82
	C ivλ1549	29.6 ± 0.8	5821.40 ± 0.01	26.34 ± 0.09	1217 ± 5	216.6 ± 4.6
	He iiλ1640	18.3 ± 1.0	6161.46 ± 0.01	21.24 ± 0.16	841 ± 10	144.6 ± 5.6
	O iii]λ1663	3.32 ± 0.48	6254.25 ± 0.32	30.40 ± 0.89	1328 ± 47	28.48 ± 1.58
	Si iiλ1814	2.77 ± 0.31	6793.44 ± 0.90	61.13 ± 6.67	2629 ± 302	24.50 ± 3.14
	C iii]λ1909	18.2 ± 1.1	7163.06 ± 0.01	29.62 ± 0.28	1085 ± 14	200.1 ± 8.0
	[O iii]+C ii+Si iiλ2322	11.1 ± 0.83	8735.29 ± 0.12	38.19 ± 1.03	1165 ± 40	216.5 ± 25.6
	[Ne iv]λ2424	6.18 ± 0.50	9104.60 ± 0.09	31.24 ± 0.44	836 ± 18	87.90 ± 3.73
4C 24.28	Ly$\alpha\lambda$1216	46.5 ± 0.4	4761.77 ± 0.03	29.93 ± 0.20	1786 ± 13	1005 ± 109
	N vλ1240	10.5 ± 0.7	4855.16 ± 0.09	32.66 ± 1.08	1925 ± 70	77.64 ± 8.34
	O i+Si iiλ1305	0.67 ± 0.15	5108.32 ± 0.17	14.72 ± 0.56	621 ± 46	9.11 ± 0.76
	Si ivλ1397+O iv]λ1402	3.34 ± 0.29	5488.64 ± 0.20	45.38 ± 2.36	2405 ± 133	47.92 ± 3.79
	N iv]λ1486	1.28 ± 0.20	5811.57 ± 0.89	39.45 ± 4.82	1943 ± 260	24.85 ± 3.23
	C ivλ1549	10.3 ± 0.4	6062.13 ± 0.06	45.03 ± 0.27	2145 ± 14	148.8 ± 3.5
	He iiλ1640	8.98 ± 0.30	6416.40 ± 0.09	28.13 ± 0.54	1169 ± 28	156.1 ± 11.5
	O iii]λ1663	2.13 ± 0.25	6510.19 ± 0.34	57.33 ± 3.02	2571 ± 143	44.63 ± 4.53
	C iii]λ1909	7.41 ± 0.61	7464.27 ± 0.23	43.17 ± 3.04	1626 ± 130	173.5 ± 32.0
	[O iii]+C ii+Si iiλ2322	0.96 ± 0.21	9106.79 ± 0.35	23.55 ± 0.76	490 ± 40	31.74 ± 2.79
USS 1545-234	Ly$\alpha\lambda$1216	18.0 ± 0.2	4563.85 ± 0.01	15.23 ± 0.12	801 ± 10	1315 ± 465
	N vλ1240	7.01 ± 0.48	4646.44 ± 0.16	37.71 ± 0.91	2358 ± 60	85.61 ± 5.74
	Si ivλ1397+O iv]λ1402	1.30 ± 0.14	5249.85 ± 0.06	23.54 ± 1.19	1202 ± 76	39.17 ± 6.87
	C ivλ1549	6.76 ± 0.30	5810.36 ± 0.02	24.77 ± 0.31	1128 ± 18	322.7 ± 29.4
	He iiλ1640	4.72 ± 0.20	6150.74 ± 0.01	16.65 ± 0.16	547 ± 12	191.7 ± 14.1
	O iii]λ1663	0.85 ± 0.13	6237.76 ± 0.16	21.29 ± 1.30	828 ± 78	38.72 ± 5.06
	C iii]λ1909	2.88 ± 0.21	7151.00 ± 0.07	26.68 ± 1.15	944 ± 57	155.6 ± 21.2
	[O iii]+C ii+Si iiλ2322	1.13 ± 0.31	8730.34 ± 0.16	19.02 ± 0.53	322 ± 41	70.83 ± 6.08
	[Ne iv]λ2424	1.72 ± 0.24	9088.72 ± 0.33	22.82 ± 1.73	446 ± 105	141.6 ± 39.8

Notes.
[a] Central wavelength.
[b] Observed wavelength width in FWHM before the correction for the instrumental broadening.
[c] Velocity width in FWHM after the correction for the instrumental broadening.

Table 3
Data of Additional Targets

Name	z	Available Emission Lines	Reference[a]
0211−122	2.340	Si iv + O iv], N iv], C iv, He ii, O iii], C iii], [Ne iv]	H08
0406−244	2.440	Si iv + O iv], C iv, He ii, O iii], C iii], [Ne iv]	H08
0731+438	2.429	Si iv + O iv], N iv], C iv, He ii, O iii], C iii], [Ne iv]	V01
0828 + 193	2.572	Si iv + O iv], N iv], C iv, He ii, O iii], C iii], [Ne iv]	H08
0943−242	2.922	Si iv + O iv], N iv], C iv, He ii, O iii], C iii]	V01
1558−003	2.479	Si iv + O iv], N iv], C iv, He ii, O iii], C iii], [Ne iv]	H08
3C 256	1.824	Si iv + O iv], C iv, He ii, O iii], C iii], [Ne iv]	S99
4C−00.54	2.360	Si iv + O iv], C iv, He ii, O iii], C iii], [Ne iv]	H08
4C+23.56	2.470	Si iv + O iv], N iv], C iv, He ii, O iii], C iii], [Ne iv]	H08
4C+40.36	2.265	Si iv + O iv], N iv], C iv, He ii, O iii], C iii], [Ne iv]	H08
4C+48.48	2.343	Si iv + O iv], N iv], C iv, He ii, O iii], C iii], [Ne iv]	V01
NVSS J002402−325253	2.043	Si iv + O iv], C iv, He ii, O iii], C iii], [Ne iv]	DB06

Note.
[a] S99 = Simpson et al. (1999); V01 = Vernet et al. (2001); DB06 = De Breuck et al. (2006); H08 = Humphrey et al. (2008). [2]Redshifts from the NASA/IPAC Extragalactic Database (NED).

Table 4
Ionization Potentials of Ions

Ion	Ionization Potential (eV)
C III	24.4
O III	35.1
Si IV	33.5
N IV	47.4
C IV	47.9
He II	54.4
O IV	54.9
Ne IV	63.5

Table 5
Comparison between Photoionization Models and Observations

Name	$\tilde{\chi}^2$	Z ($Z_\odot$)	log n (cm^{-3})	log U
TN J0920−0712	3.79	$1.2^{+0.1}_{-0.2}$	$4.4^{+0.2}_{-0.2}$	$-1.7^{+0.1}_{-0.1}$
4C 24.28	13.19	$2.1^{+0.2}_{-0.9}$	$5.3^{+0.1}_{-0.9}$	>-1.7[a]
USS 1545−234	9.93	$1.4^{+0.2}_{-0.2}$	$4.3^{+0.2}_{-0.2}$	$-1.4^{+0.2}_{-0.1}$
0211−122	12.34	$1.4^{+0.1}_{-0.1}$	$3.7^{+0.2}_{-0.2}$	$-1.3^{+0.1}_{-0.2}$
0406−244	6.01	$2.0^{+2.7}_{-0.6}$	$4.4^{+1.2}_{-0.5}$	>-2.0[a]
0731 + 438	15.29	$0.7^{+0.0}_{-0.1}$	<2.4[a]	$-1.5^{+0.0}_{-0.1}$
0828 + 193	12.94	$0.7^{+0.1}_{-0.0}$	<2.2[a]	$-1.4^{+0.1}_{-0.1}$
0943−242	7.39	$0.9^{+0.0}_{-0.1}$	<2.3[a]	$-1.6^{+0.1}_{-0.1}$
1558−003	5.51	$0.7^{+0.2}_{-0.1}$	$4.2^{+0.3}_{-0.6}$	$-1.5^{+0.1}_{-0.1}$
3C 256	27.05	$1.3^{+0.1}_{-0.3}$	$4.1^{+0.2}_{-0.3}$	$-1.8^{+0.1}_{-0.1}$
4C−00.54	31.32	$1.4^{+0.1}_{-0.2}$	$4.2^{+0.2}_{-0.3}$	$-1.0^{+0.1}_{-0.2}$
4C+23.56	18.44	$1.1^{+0.3}_{-0.2}$	$3.3^{+0.7}_{-0.4}$	$-1.5^{+0.1}_{-0.1}$
4C+40.36	10.99	$0.6^{+0.0}_{-0.1}$	<2.1[a]	$-1.9^{+0.1}_{-0.0}$
4C+48.48	13.80	$1.3^{+0.2}_{-0.1}$	$3.9^{+0.2}_{-0.3}$	$-1.6^{+0.1}_{-0.1}$
J0024−3252	5.12	$1.6^{+0.3}_{-0.2}$	$4.3^{+0.1}_{-0.2}$	$-1.8^{+0.1}_{-0.1}$

Note.
[a] The cases reaching the upper/lower limit of the parameter ranges in our model runs.

observations because of the uncertainty of the acquisition onto the slit position and slit loss depending on the seeing condition. Moreover, our observations were mostly performed in worse seeing conditions in which the typical seeing was 1.″4. Thus the measurement accuracy was worse due to slit loss. As another error cause, we measured the line fluxes by fitting with a single Gaussian profile to each line. However, some emission lines show asymmetric profiles and deviations from the ideal Gaussian profile (Figures 1–3), and thus the measured fluxes are incomplete and do not represent the actual fluxes. In order to correct these errors, we conservatively adopt the 1σ flux error to be 10% for emission lines detected with S/N > 10 in the following χ^2 calculations.

We perform the minimum $\tilde{\chi}^2$ search 10,000 times using observed emission-line flux ratios. In each search, we vary the emission-line flux ratios randomly within the 1σ flux error of the observed line-flux ratios to evaluate the scatter of the ISM parameters. The best-fit parameters are determined by the median value of the minimum $\tilde{\chi}^2$ in the search. The errors of parameters are estimated by the 18 and 84 percentile values of the distribution of the minimum χ^2. The obtained median of the minimum $\tilde{\chi}^2$ and best-fit parameters are summarized in Table 5 for 15 HzRGs in our sample.

In order to understand which emission-line ratio is the most important to determine each ISM parameter, we check the behavior of each flux ratio as a function of the ISM parameters. Figure 4 shows the dependence of the flux ratios on the metallicity, where the models are calculated with parameter sets of log $U = -3.0$, -2.0, -1.0, and -0.5, and log $n =$ 2.0, 4.0, and 6.0. All line ratios increase with increasing gas density from log $n = 2.0$ to 6.0 (i.e., from the left to the right panel), especially in models with a higher metallicity. These trends suggest that the gas density is closely related to almost all line ratios. This density dependence of C IV/He II in NLRs has been reported in earlier works (e.g., Nagao et al. 2006b). It is natural that the [Ne IV]/He II line ratio shows a positive dependence on the gas density because the [Ne IV] line is a forbidden emission with a critical density of log $n_{\rm cr} \sim 5.0$ (the [Ne IV] line is an unresolved doublet emission of [Ne IV]λ2422 and [Ne IV] λ2425 with log $n_{\rm cr} =$ 5.4 and 4.9, respectively; see, e.g., Zheng 1988). All line ratios also show the dependence on metallicity in the low gas density models (log $n = 2.0$), while the metallicity dependence seems to be weaker in the higher gas density models. This trend infers that gas density and metallicity are degenerate; i.e., a high flux ratio is due to either a high gas density or a high metallicity, or both. Thus the constraint on the gas density is important for estimating the metallicity accurately. Figure 4 also suggests that the ionization parameter is constrained by combining Si IV+O IV]/He II, N IV]/He II, C II/He II, and [Ne IV]/He II, i.e., the flux ratios of two emission lines with different ionization potentials. These line ratios increase with decreasing ionization parameter.

The dependence of the gas density on the C III]/He II flux ratio is thought to be small, while that of C IV/He II is not small (e.g., Nagao et al. 2006b; Matsuoka et al. 2009). Although these emission-line flux ratios have been used to discuss the metallicity of NLR clouds by assuming a certain gas density, the uncertainty of the gas density in the estimation of the metallicity had not been discussed in detail. Figure 4 shows that the C IV/He II flux ratio depends on the gas density by at most 2 dex from log $n = 2$–6 at the highest metallicity model, and thus the previous metallicity measurement may be affected by this density dependence. For example, the C IV/He II flux ratio of TN J0920−0712 is 1.617. This corresponds to $\sim 1.5\,Z_\odot$ assuming a model with log $n = 4.0$ and log $U = -1$, while the metallicity is inferred to be $\sim 5\,Z_\odot$ with the log $n = 6.0$ model. In this work, the density is well determined with an accuracy within 0.3 dex in most cases thanks to constraints from many weak emission lines, and thus the metallicity of each target can be estimated with a smaller uncertainty than previous studies that were based on only a few emission lines. For example, Matsuoka et al. (2009) estimated an NLR metallicity with 0.2–0.8 dex uncertainty, even in averaged values.

5. Discussion

5.1. Interpretations of the Model Fitting

The best-fit photoionization models suggest that many objects in our sample show higher gas metallicities than solar ($Z \gtrsim 1.0\ Z_\odot$). These inferred metallicities are consistent with earlier works for HzRGs (De Breuck et al. 2000; Nagao et al. 2006b; Matsuoka et al. 2009). This result suggests that the NLRs of HzRGs in our sample are already chemically mature even at $z > 3$. The inferred ionization parameter is $-2.0 <$ log $U < -1.0$ in our sample. De Breuck et al. (2000) and Bryant et al. (2009) reported that the ionization parameter of HzRGs is in the range of $-2.5 <$ log $U < -1.5$ using rest-UV

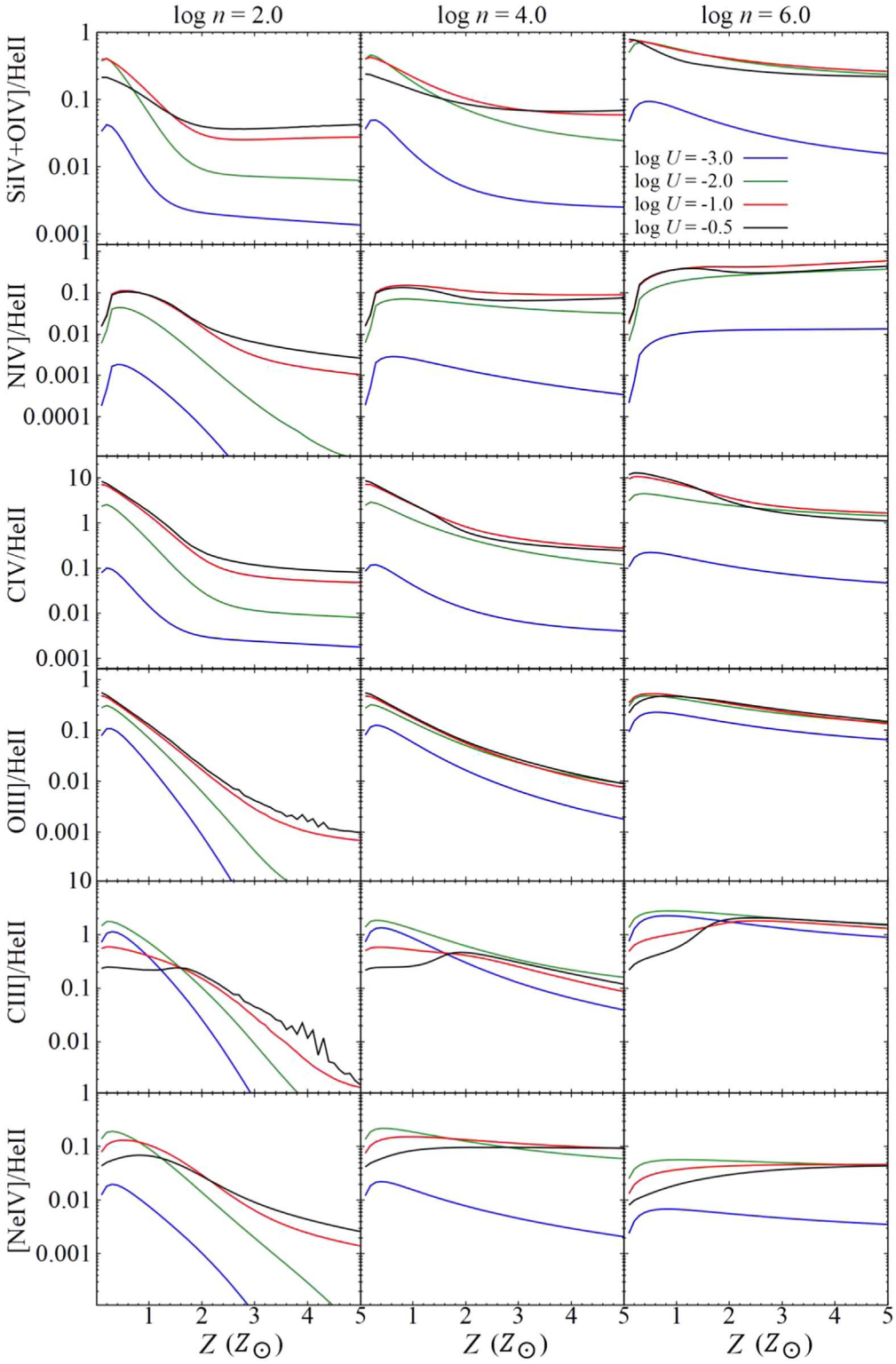

Figure 4. The relation between the predicted flux ratio and metallicity. From left to right, models with log $n = 2$, 4, and 6 are shown. The blue, green, red, and black lines denote the results with log $U = -3$, -2, -1, and -0.5, respectively.

emission-line ratios and photoionization models assuming solar metallicity and gas density (log $n = 2.0$ and 3.0). The ionization parameter in our work is distributed in a range slightly higher than the range reported in these previous works, but the difference is insignificant within the uncertainty of the estimation. The inferred gas density of HzRGs is widely distributed in the range of log $n = 2.0$–5.0 with a relatively larger uncertainty than the derived uncertainty in the ionization parameter and gas metallicity. The inferred range of the gas density is consistent with the range of the gas density assumed in the previous works (e.g., De Breuck et al. 2000; Nagao et al. 2006b; Matsuoka et al. 2009). Humphrey et al. (2008) determined an electron density of 0731 + 438 and log $n_e < 3.5$ by using [Si III]λ1883/Si III]λ1892. This result is consistent with our results (log $n_e < 2.4$).

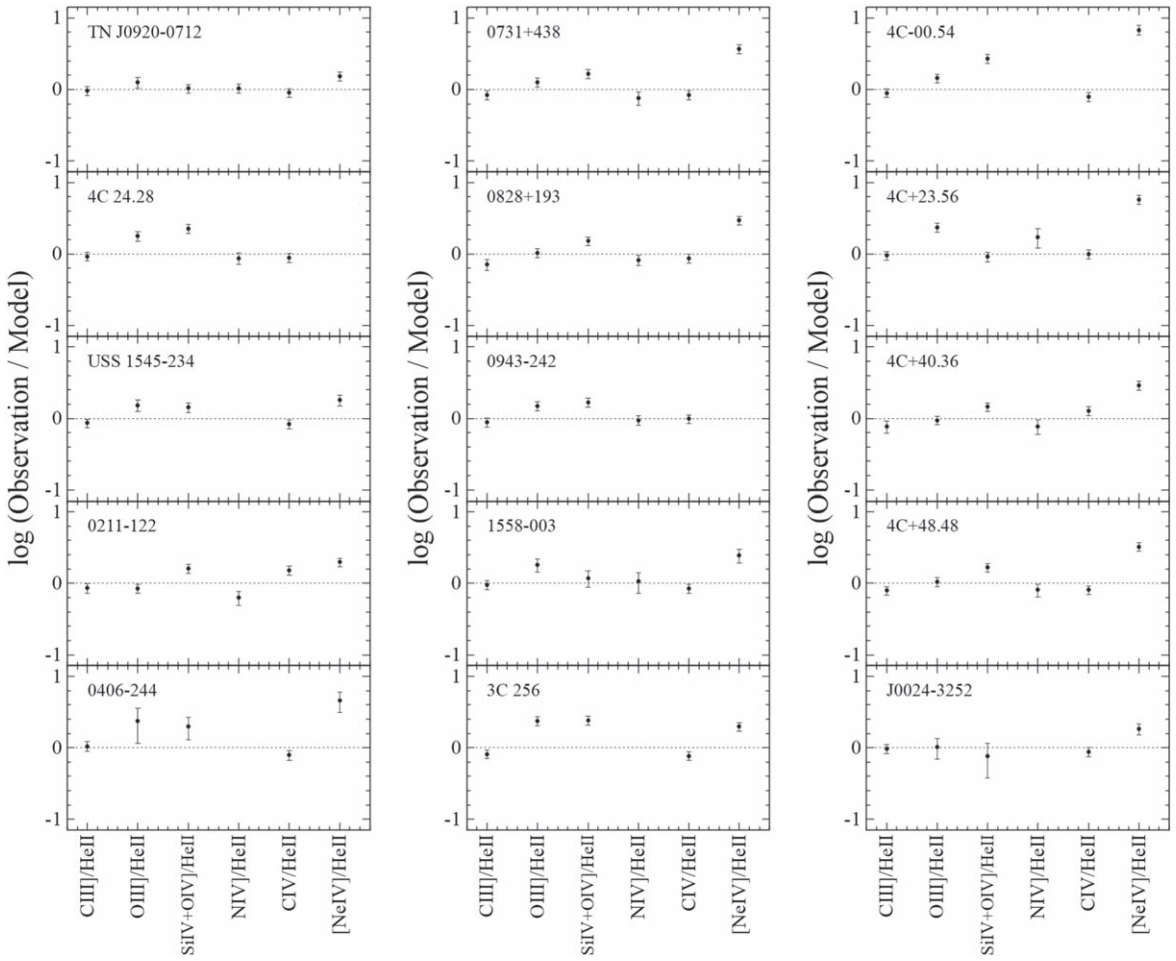

Figure 5. Comparison of each emission-line flux ratio between photoionization models and observations at the minimum $\tilde{\chi}^2$. In the *x*-axis, the flux ratios are shown in order of increasing ionization potential of the corresponding ion (of the numerator), from left to right. The dashed line indicates unity, i.e., the observed flux ratios are reproduced by best-fit models.

Table 6
Line Luminosities and Radio Power

Name	log $L_{\rm CIV}$ (erg s^{-1})	log $L_{\rm HeII}$ (erg s^{-1})	log P_{365}[a] (erg s^{-1} Hz^{-1})	log P_{1400}[b] (erg s^{-1} Hz^{-1})
J0920−0712	43.27 ± 0.01	43.06 ± 0.02	35.68 ± 0.02	34.80 ± 0.01
4C 24.28	42.87 ± 0.02	42.81 ± 0.01	36.30 ± 0.01	35.60 ± 0.01
USS 1545−234	42.63 ± 0.02	42.47 ± 0.02	35.87 ± 0.01	35.23 ± 0.01
0211−122	42.44 ± 0.01	42.18 ± 0.01	35.63 ± 0.01	34.99 ± 0.02
0406−244	42.63 ± 0.05	42.75 ± 0.04	36.26 ± 0.01	35.47 ± 0.01
0731 + 438	43.33 ± 0.01	43.15 ± 0.01	36.12 ± 0.01	35.55 ± 0.01
0828 + 193	43.38 ± 0.01	43.14 ± 0.01	35.47 ± 0.02	34.80 ± 0.01
0943−242	43.53 ± 0.01	43.53 ± 0.01	35.99 ± 0.02	35.29 ± 0.01
1558−003	43.09 ± 0.02	42.66 ± 0.01	35.96 ± 0.01	35.33 ± 0.01
3C 256	43.08 ± 0.01	43.10 ± 0.01	36.10 ± 0.01	35.50 ± 0.01
4C−00.54	42.18 ± 0.03	42.04 ± 0.01	35.61 ± 0.03	35.00 ± 0.02
4C+23.56	41.94 ± 0.05	41.86 ± 0.03	35.99 ± 0.02	35.52[c]
4C+40.36	42.43 ± 0.02	42.18 ± 0.03	36.09 ± 0.01	35.29 ± 0.01
4C+48.48	43.37 ± 0.01	43.35 ± 0.03	35.87 ± 0.02	35.19 ± 0.01
J0024−3252	42.50 ± 0.05	42.50 ± 0.05	...	34.10 ± 0.01

Notes.
[a] The 365 MHz flux data were collected from Douglas et al. (1996).
[b] The 1400 MHz flux data were collected from Condon et al. (1998).
[c] This 1400 MHz flux density is collected from White & Becker (1992).

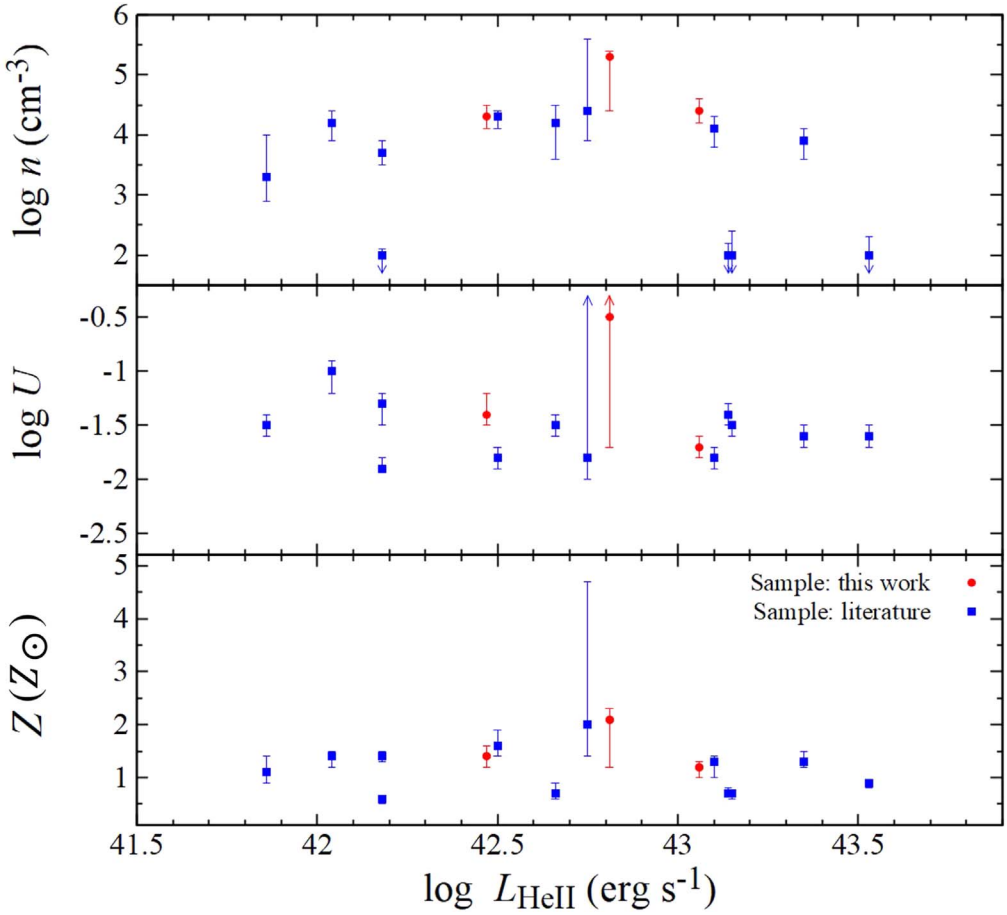

Figure 6. Inferred parameters (gas density, ionization parameter, and gas metallicity in the upper, middle, and lower panels, respectively) as a function of the He II luminosity. Red circles are our targets, and blue squares are HzRGs taken from the literature. Arrows denote the cases where the inferred error reaches the calculation limit.

Silva et al. (2018) examined photoionization models to study the rest-frame UV and optical emission-line spectrum of 0943−242, which is included in our sample. Their best-fit parameters are $Z = 2.1\ Z_{\odot}$ and $\log U = -1.74$. The derived ionization parameter is close to the best-fit value in our analysis ($\log U = -1.6^{+0.1}_{-0.1}$), while the derived metallicity is higher than our measurement ($Z = 0.9^{+0.0}_{-0.1}\ Z_{\odot}$). Note that in their one-zone cloud models, the hydrogen gas density was fixed to $\log n = 2.0$. However, Figure 4 shows that most flux ratios of rest-frame UV emission lines show a significant dependence on the gas density, and thus the fixed gas density may result in a possibly large systematic error in the estimates of parameters such as the metallicity. In addition, in their fit to derive the best-fit parameters, they used not only high-ionization lines, but also some low-ionization lines (C II]λ2326, Mg IIλ2798, and [O II] λ3727). Since high-ionization lines and low-ionization lines generally arise in different parts in the NLR (e.g., Ferguson et al. 1997), comparisons of such diverse emission lines with one-zone photoionization models may introduce non-negligible systematic errors. These two aspects may be the reasons for the discrepancy in the metallicity estimate for 0943−242 between Silva et al. (2018) and our work.

As shown in Table 5, the best-fit $\tilde{\chi}^2$ value in some cases is relatively large ($\gtrsim$20). This large $\tilde{\chi}^2$ is caused probably by the oversimplification of our photoionization models. In our model calculations, we assumed a constant chemical composition without dust grains, a typical AGN SED, and one-zone constant-density clouds. Although our models focus only on relatively high ionization lines, the models still suffer from this nonuniformity of NLRs, which could make the minimum $\tilde{\chi}^2$ values considerably high.

Figure 5 shows the difference in emission-line flux ratios between the observed data and the best-fit photoionization model. In most cases, the observed C III]/He II and C IV/He II flux ratios are consistent with the model predictions within the uncertainty, while [Ne IV]/He II flux ratios are systematically underpredicted by the best-fit models. One possible explanation of this discrepancy is the higher ionization potential of Ne IV (63.5 eV) compared to the other emission lines (Table 4).[8] Given the stratified structure of actual NLRs, there could be additional highly ionized clouds in the inner part of NLRs (e.g., Ferguson et al. 1997; Nagao et al. 2001a, 2001b; Rose et al. 2015; Adhikari et al. 2016) that are not taken into account in our one-zone photoionization model.

As mentioned in Section 2.1, we assume that the internal dust extinction is negligible for our HzRGs samples. In order to see the effect of this assumption, we perform the χ^2 fitting by using extinction-corrected emission-line flux ratios. In this test, we assume $A_V = 0.5$, the Cardelli et al. (1989) extinction curve, and

[8] The ionization potentials shown in Table 4 are the value required to create the ions needed to emit each emission line. Note that He II is a recombination line, so the creation of the He^{2+} ion is required to radiate the He II line. On the other hand, the other emission lines are collisionally excited lines, which do not require the presence of ions that are ionized to the higher ionization level.

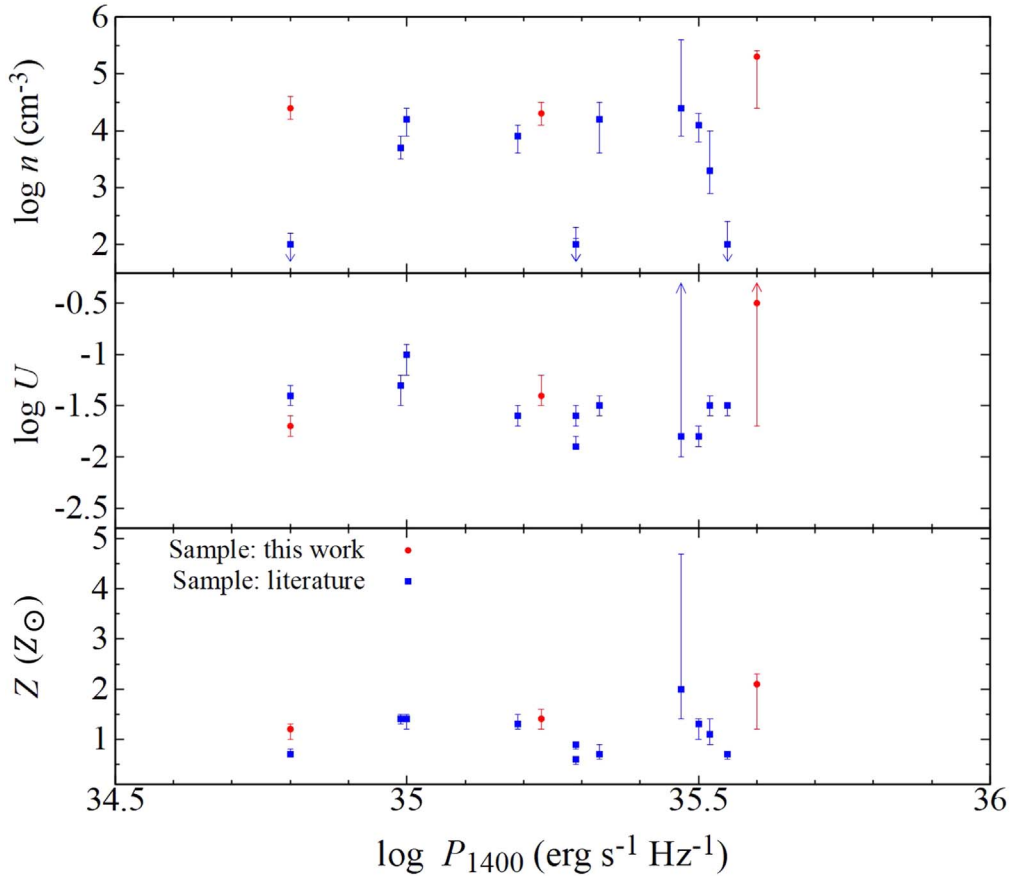

Figure 7. Relation between the radio power at 1400 MHz (P_{1400}) and the derived NLR parameters, i.e., the gas density (upper), ionization parameter (middle), and metallicity (lower). Red circles denote our targets. Blue squares denote additional HzRG samples from the literature. Arrows denote the cases where the inferred error reaches the limit of calculations.

$R_V = 3.1$. As a result, the obtained best-fit parameters of the ISM are almost consistent within a 1σ error with the results without extinction correction. This suggests that the ISM parameters inferred by the comparison with photoionization models are not sensitive to the assumption on the dust extinction.

It has been reported that the ionizing radiation of some AGNs shows significant variability on a relatively short timescale ($\lesssim 10^4$ yr), and consequently, the ionization of NLRs in such AGNs can be largely affected (e.g., Ichikawa et al. 2019; see also Bland-Hawthorn et al. 2013; Gnat 2017; Bland-Hawthorn et al. 2019). Such a short flare-like variability will cause inhomogeneous ionization structures of NLRs, which is hard to describe by one-zone photoionization models as given in this paper. Multizone photoionization models for NLRs (e.g., Ferguson et al. 1997) may be useful to investigate these inhomogeneous structures of NLRs in high-z AGNs, including HzRGs. Since multizone photoionization models involve more free parameters than one-zone photoionization models generally, studies of the inhomogeneity of high-z NLRs require many more emission lines (more than the lines in this paper; i.e., >10). Thus a wider spectroscopic coverage including the near-infrared (i.e., rest-frame optical) will be important for a detailed understanding of the ISM in high-z AGNs.

5.2. The Nature of HzRGs

Here we investigate possible dependences of the derived parameters of NLR clouds on the AGN luminosity. In Table 6, the C IV and He II emission-line luminosities of our sample are summarized. Both of the two line luminosities have often been used as indicators of the AGN luminosity, but the He II luminosity is a better indicator of the AGN activity (see Section 4). The derived parameters of NLR clouds, i.e., the gas density, ionization parameter, and metallicity, are shown as functions of the He II luminosity in Figure 6. From Spearman's rank-correlation test, the obtained correlation coefficients of the gas density, ionization parameter, and metallicity to the He II luminosity are −0.18, −0.18, and −0.20, respectively. These values suggest that these parameters do not significantly depend on the He II luminosity. This is interesting because some previous studies reported the dependence of the NLR metallicity on the AGN luminosity (e.g., Nagao et al. 2006b; Matsuoka et al. 2009). Note that this luminosity dependence of the AGN metallicity has also been reported for BLR clouds (e.g., Hamann & Ferland 1993; Nagao et al. 2006c; Matsuoka et al. 2011b). The lack of a significant luminosity dependence of the NLR metallicity in our sample is probably due to the small coverage of the luminosity and the small number statistics of our work; in previous works, the luminosity dependence of the NLR metallicity was investigated based on averaged values of a larger sample that consisted of ∼50 HzRGs (see Nagao et al. 2006b; Matsuoka et al. 2009). The luminosity coverage of the sample in Matsuoka et al. (2009) is $41.5 < \log L_{\rm HeII} < 45.0$, while our work misses luminous samples ($43.5 < \log L_{\rm HeII} < 45.0$) that have a higher metallicity than less luminous samples. As a result, the luminosity dependence may have disappeared in our sample.

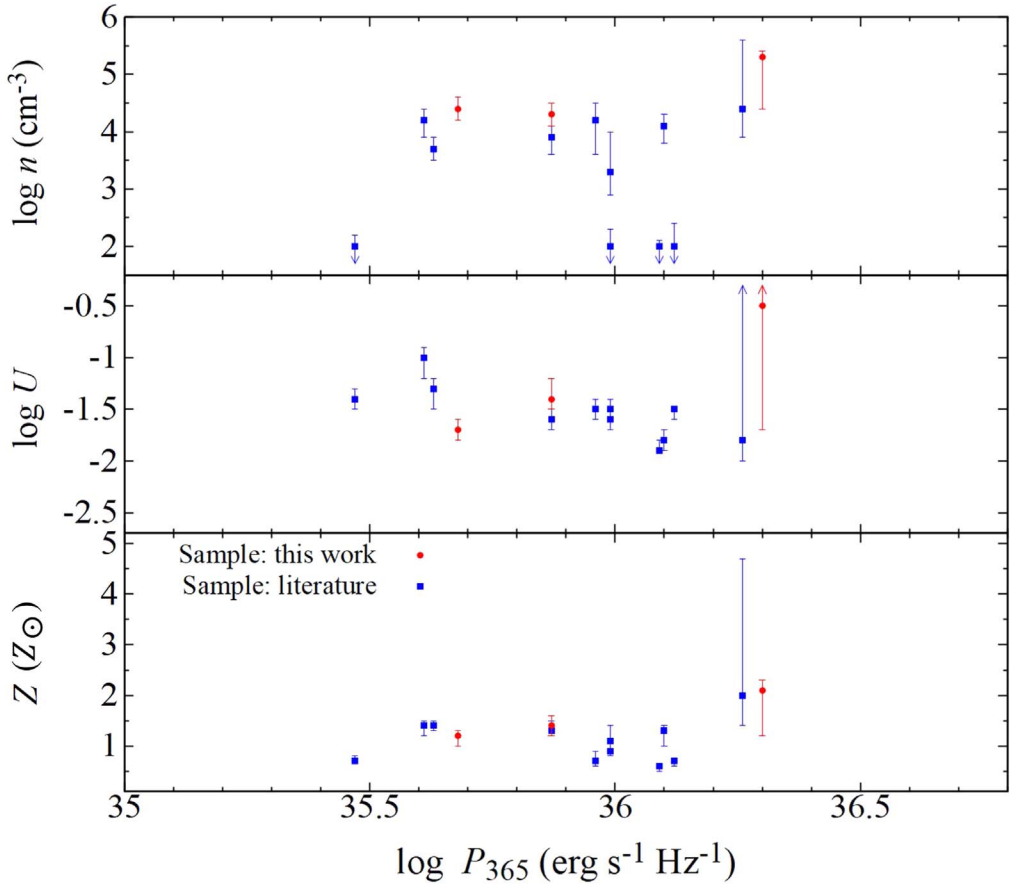

Figure 8. Same as Figure 7, but for the radio power at 365 MHz (P_{365}).

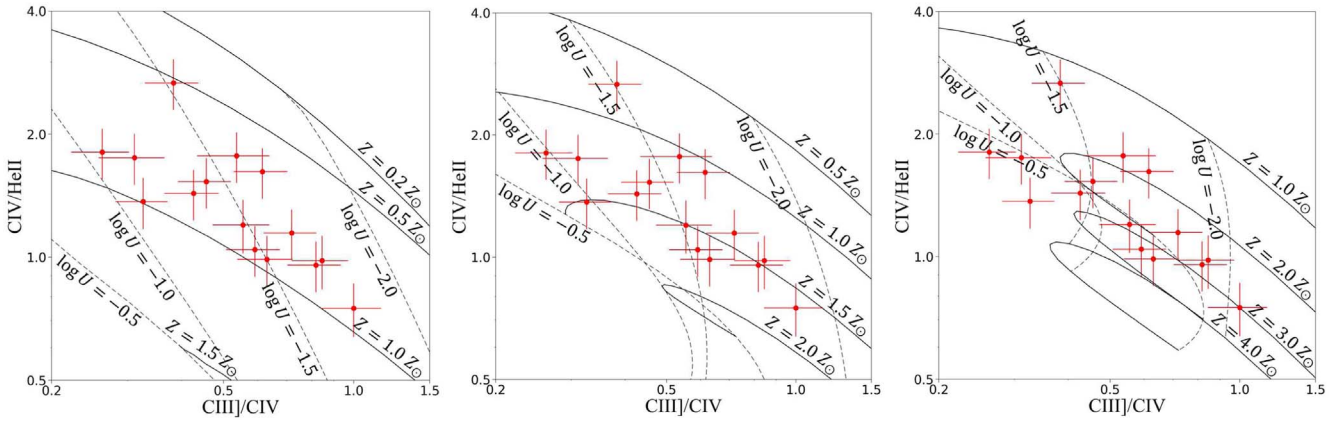

Figure 9. C III]/C IV vs. C IV/He II diagram with photoionization model grids. The left, middle, and right panels show models with log $n_{\rm H}$ = 2.0, 4.0, and 5.0, respectively. The observed line ratios of our targets are plotted with red circles.

We also examine the dependence of the NLR parameters on the radio power, in order to investigate whether some NLR parameters are strongly affected by the radio jet in HzRGs. For this purpose, we compiled the radio power at 365 MHz (P_{365}) and 1400 MHz (P_{1400}) summarized in Table 6, which are taken from White & Becker (1992), Douglas et al. (1996), and Condon et al. (1998). The relation between the NLR parameters and the radio power is shown in Figures 7 and 8. From Spearman's rank-correlation test, the obtained correlation coefficients of the gas density, ionization parameter, and metallicity to the radio power are 0.17, −0.37, and 0.11 for P_{365}, and 0.01, −0.22, and −0.05 for P_{1400}, respectively. From these results, the ionization parameter might be weakly correlated with P_{365}. The other ISM parameters do not show a significant dependence on the radio power. These figures and the rank-correlation test suggest that there is no clear dependence of the NLR parameters on the radio power, suggesting that the physical properties of NLRs in our sample are not significantly affected by the radio jet. This is consistent with the idea that the NLR clouds of AGNs in our samples are mostly ionized by the photoionization, not by the fast shock associated with the radio jet. However, in order to conclude

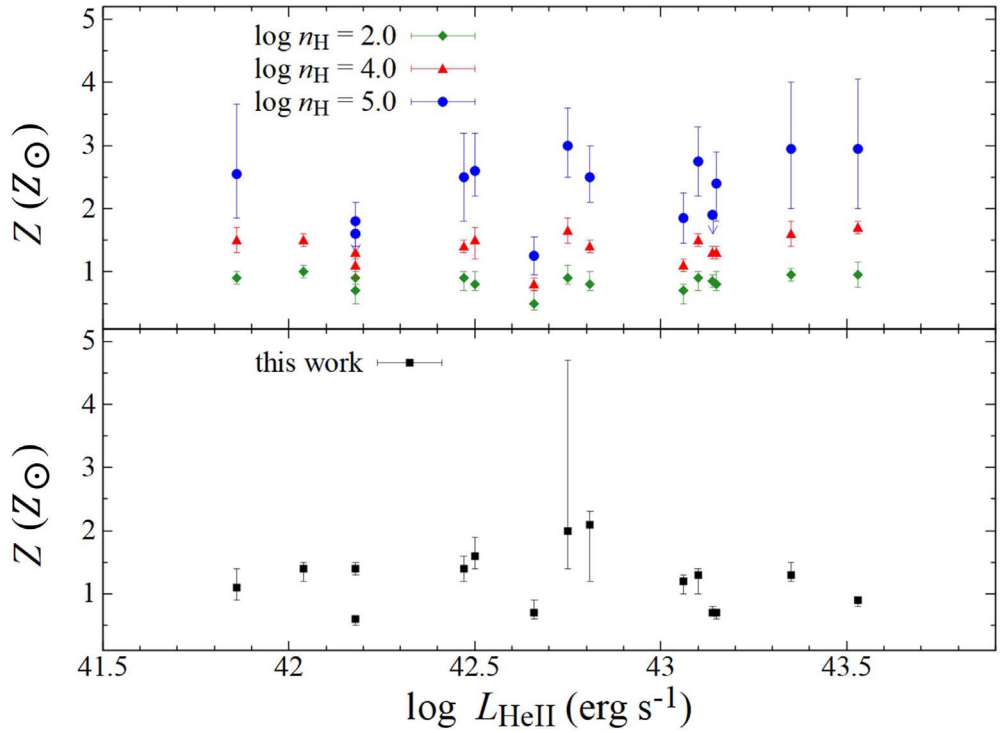

Figure 10. Inferred metallicity of our targets estimated with the line diagnostics with only strong emission lines (top panel) and with our method (bottom panel), as a function of the He II line luminosity. In the top panel, the green diamond, red triangle, and blue circle represent the metallicity estimated with models with log n_H = 2.0, 4.0, and 5.0, respectively.

Table 7
Estimated Gas-phase Metallicity[a] with Different Models

Name	This Work Best Fit	M+09[b] log n_H = 2.0	M+09 log n_H = 4.0	M+09 log n_H = 5.0
J0920−0712	$1.2^{+0.1}_{-0.2}$	$0.7^{+0.1}_{-0.2}$	$1.1^{+0.1}_{-0.1}$	$1.85^{+0.4}_{-0.4}$
4C 24.28	$2.1^{+0.2}_{-0.9}$	$0.8^{+0.2}_{-0.1}$	$1.4^{+0.1}_{-0.1}$	$2.5^{+0.5}_{-0.4}$
USS 1545−234	$1.4^{+0.2}_{-0.2}$	$0.9^{+0.1}_{-0.2}$	$1.4^{+0.1}_{-0.1}$	$2.5^{+0.7}_{-0.3}$
0211−122	$1.4^{+0.1}_{-0.1}$	$0.9^{+0.1}_{-0.2}$	$1.3^{+0.1}_{-0.1}$	<1.6
0406−244	$2.0^{+2.7}_{-0.6}$	$0.9^{+0.2}_{-0.1}$	$1.65^{+0.2}_{-0.2}$	$3.0^{+0.6}_{-0.5}$
0731 + 438	$0.7^{+0.0}_{-0.1}$	$0.8^{+0.2}_{-0.1}$	$1.3^{+0.1}_{-0.1}$	$2.4^{+0.5}_{-0.6}$
0828 + 193	$0.7^{+0.1}_{-0.0}$	$0.85^{+0.1}_{-0.1}$	$1.3^{+0.1}_{-0.1}$	<1.9
0943−242	$0.9^{+0.0}_{-0.1}$	$0.95^{+0.2}_{-0.2}$	$1.7^{+0.1}_{-0.1}$	$2.95^{+1.1}_{-0.95}$
1558−003	$0.7^{+0.2}_{-0.1}$	$0.5^{+0.2}_{-0.1}$	$0.8^{+0.1}_{-0.1}$	$1.25^{+0.3}_{-0.3}$
3C 256	$1.3^{+0.1}_{-0.3}$	$0.9^{+0.1}_{-0.2}$	$1.5^{+0.1}_{-0.1}$	$2.75^{+0.55}_{-0.55}$
4C−00.54	$1.4^{+0.1}_{-0.2}$	$1.0^{+0.1}_{-0.1}$	$1.5^{+0.1}_{-0.1}$	⋯
4C+23.56	$1.1^{+0.3}_{-0.2}$	$0.9^{+0.1}_{-0.1}$	$1.5^{+0.2}_{-0.2}$	$2.55^{+1.1}_{-0.7}$
4C+40.36	$0.6^{+0.0}_{-0.1}$	$0.7^{+0.1}_{-0.2}$	$1.1^{+0.2}_{-0.2}$	$1.8^{+0.3}_{-0.4}$
4C+48.48	$1.3^{+0.2}_{-0.1}$	$0.95^{+0.1}_{-0.1}$	$1.6^{+0.2}_{-0.2}$	$2.95^{+1.05}_{-0.95}$
J0024−3252	$1.6^{+0.3}_{-0.2}$	$0.8^{+0.2}_{-0.1}$	$1.5^{+0.2}_{-0.3}$	$2.6^{+0.6}_{-0.4}$

Notes.
[a] Given in units of solar metallicity.
[b] Matsuoka et al. (2009).

about the influence of radio jets, it is necessary to investigate the spatial distributions between radio jets and line-emitting clouds (Tadhunter et al. 2000; Nesvadba et al. 2017).

The obtained NLR metallicity for our sample is distributed in the range of 0.5–2.1 $Z_\odot$ (Figure 6); i.e., the NLR of most HzRGs in our sample is characterized by solar or supersolar metallicity. This suggests that host galaxies of HzRGs are chemically mature even at $z \sim 3$, where the average and standard deviation of the stellar mass of our HzRG sample (0406−244, 0943−242, 1558−003, 4C+23.56, and 4C +40.36) is $(2.7 \pm 1.3) \times 10^{11} M_\odot$ (Seymour et al. 2007; De Breuck et al. 2010). As a comparison of the same stellar mass of HzRGs, local galaxies with $\sim 10^{11} M_\odot$ also have solar or supersolar metallicity (e.g., Tremonti et al. 2004; Maiolino & Mannucci 2019; Curti et al. 2020). Some earlier works (e.g., Nagao et al. 2006b; Matsuoka et al. 2009) pointed out that the NLR metallicity of HzRGs is solar or supersolar, but with some assumptions on the NLR gas parameters (e.g., a fixed gas density). In this work, the chemical maturity of HzRGs is confirmed with fewer assumptions thanks to deep spectra with weak emission lines.

5.3. Comparison with Diagnostics Using Only Strong Lines

To examine whether our multiline assessment including faint lines is better than previous strong-line diagnostics, we compare the inferred NLR metallicity of HzRGs in this work (Table 5) with the metallicity estimated with only strong lines. Nagao et al. (2006b) and Matsuoka et al. (2009) estimated the NLR metallicity by using the emission-line flux ratios of C IV/He II and C III]/C IV. Figure 9 shows the strong-line metallicity diagnostic diagram that consists of the flux ratios of C IV/He II and C III]/C IV for the cases of log $n_H = 2.0$, 4.0, and 5.0, with the grid of Cloudy photoionization models.[9] The resulting metallicity based on the strong-line diagnostic diagram is given in Figure 10 and Table 7, with the metallicity estimated by our multiline assessment (Section 4). Figure 10 shows that the strong-line method has a large (a factor of ∼2–3) systematic uncertainty

[9] Details of the model calculations are given in Section 4.1; note that we use Cloudy version 13.03, although Matsuoka et al. (2009) used version 07.02.

associated with the gas density, given the fact that we have to assume one specific density to use the strong-line metallicity diagnostic diagram. On the other hand, our multiline assessment estimates the metallicity, gas density, and ionization parameter simultaneously. The resulting error is typically 0.3 dex, which is smaller than the systematic uncertainty in the strong-line method. Therefore, we conclude that our multiline assessment using rest-UV faint emission lines is more powerful for studying the NLR metallicity than previous strong-line methods.

6. Conclusion

In this work, we focus on rest-frame UV emission lines including faint ones (such as N IV]λ1486, O III]λ1663, and [Ne IV]λ2424) of 15 HzRGs at $z \sim 3$ in order to examine the ISM properties (gas density, ionization parameter, and metallicity) of NLRs in HzRGs. We diagnose the physical and chemical properties of the ISM in NLR for each object through the comparison between the observed emission-line fluxes and detailed photoionization models. The main results of this work are as follows.

1. Most HzRGs show a high gas metallicity that is close to or higher than the solar metallicities (i.e., $Z \gtrsim Z_{\odot}$). This result is consistent with some previous studies (e.g., Nagao et al. 2006b; Matsuoka et al. 2009), but was obtained with fewer assumptions in the photoionization model with respect to these previous works. The obtained result strongly suggests that HzRGs at $z \sim 3$ are already mature chemically, even in the early universe, when the cosmic age was only $\sim$2 Gyr.
2. The inferred physical parameters (gas density, ionization parameter, and gas metallicity) of NLRs in HzRGs show no correlation with the radio power. This suggests that the ionization state of the NLR gas in our sample is not significantly affected by the radio jet.

We would like to thank Gary J. Ferland for providing the photoionization code Cloudy to the public. We also thank Dr. Mitsuru Kokubo for useful comments and suggestions that improved this manuscript. Photoionization model calculations were in part carried out on the Multi-wavelength Data Analysis System operated by the Astronomy Data Center (ADC), National Astronomical Observatory of Japan. This research has made use of the NASA/IPAC Extragalactic Database (NED), which is operated by the Jet Propulsion Laboratory, California Institute of Technology, under contract with the National Aeronautics and Space Administration. K.T. was financially supported by JSPS (19K23452). T.N. was financially supported by JSPS (19H00697, 20H01949, and 21H04496).

ORCID iDs

Koki Terao https://orcid.org/0000-0001-5899-9185
Tohru Nagao https://orcid.org/0000-0002-7402-5441
Masayuki Akiyama https://orcid.org/0000-0002-2651-1701
Yoshiki Matsuoka https://orcid.org/0000-0001-5063-0340
Takuji Yamashita https://orcid.org/0000-0002-4999-9965

References

Adhikari, T. P., Różańska, A., Czerny, B., Hryniewicz, K., & Ferland, G. J. 2016, ApJ, 831, 68
Allen, M. G., Groves, B. A., Dopita, M. A., Sutherland, R. S., & Kewley, L. J. 2008, ApJS, 178, 20
Appenzeller, I., Fricke, K., Fürtig, W., et al. 1998, Msngr, 94, 1
Belfiore, F., Maiolino, R., & Bothwell, M. 2016, MNRAS, 455, 1218
Bicknell, G. V., Dopita, M. A., Tsvetanov, Z. I., & Sutherland, R. S. 1998, ApJ, 495, 680
Binette, L., Wilson, A. S., & Storchi-Bergmann, T. 1996, A&A, 312, 365
Bland-Hawthorn, J., Maloney, P. R., Sutherland, R., et al. 2019, ApJ, 886, 45
Bland-Hawthorn, J., Maloney, P. R., Sutherland, R. S., & Madsen, G. J. 2013, ApJ, 778, 58
Bryant, J. J., Johnston, H. M., Broderick, J. W., et al. 2009, MNRAS, 395, 1099
Cardelli, J. A., Clayton, G. C., & Mathis, J. S. 1989, ApJ, 345, 245
Condon, J. J., Cotton, W. D., Greisen, E. W., et al. 1998, AJ, 115, 1693
Curti, M., Cresci, G., Mannucci, F., et al. 2017, MNRAS, 465, 1384
Curti, M., Mannucci, F., Cresci, G., & Maiolino, R. 2020, MNRAS, 491, 944
De Breuck, C., Hunstead, R. W., Sadler, E. M., Rocca-Volmerange, B., & Klamer, I. 2004, MNRAS, 347, 837
De Breuck, C., Klamer, I., Johnston, H., et al. 2006, MNRAS, 366, 58
De Breuck, C., Röttgering, H., Miley, G., van Breugel, W., & Best, P. 2000, A&A, 362, 519
De Breuck, C., Seymour, N., Stern, D., et al. 2010, ApJ, 725, 36
Dopita, M. A., Kewley, L. J., Heisler, C. A., & Sutherland, R. S. 2000, ApJ, 542, 224
Dors, O. L., Cardaci, M. V., Hägele, G. F., & Krabbe, Â. C. 2014, MNRAS, 443, 1291
Douglas, J. N., Bash, F. N., Bozyan, F. A., Torrence, G. W., & Wolfe, C. 1996, AJ, 111, 1945
Erb, D. K. 2008, ApJ, 674, 151
Feltre, A., Charlot, S., & Gutkin, J. 2016, MNRAS, 456, 3354
Ferguson, J. W., Korista, K. T., Baldwin, J. A., & Ferland, G. J. 1997, ApJ, 487, 122
Ferland, G. J., Porter, R. L., van Hoof, P. A. M., et al. 2013, RMxAA, 49, 137
Förster Schreiber, N. M., Genzel, R., Bouché, N., et al. 2009, ApJ, 706, 1364
Gnat, O. 2017, ApJS, 228, 11
Goodrich, R. W., Cohen, M. H., & Putney, A. 1995, PASP, 107, 179
Greene, J. E., & Ho, L. C. 2005, ApJ, 627, 721
Grevesse, N., Asplund, M., Sauval, A. J., & Scott, P. 2010, Ap&SS, 328, 179
Groves, B. A., Dopita, M. A., & Sutherland, R. S. 2004, ApJS, 153, 75
Gu, Q., Melnick, J., Cid Fernandes, R., et al. 2006, MNRAS, 366, 480
Hamann, F., & Ferland, G. 1993, ApJ, 418, 11
Heard, C. Z. P., & Gaskell, C. M. 2016, MNRAS, 461, 4227
Ho, L. C., Filippenko, A. V., & Sargent, W. L. W. 2003, ApJ, 583, 159
Humphrey, A., Villar-Martín, M., Vernet, J., et al. 2008, MNRAS, 383, 11
Ichikawa, K., Ueda, J., Bae, H.-J., et al. 2019, ApJ, 870, 65
Izotov, Y. I., Stasińska, G., Meynet, G., Guseva, N. G., & Thuan, T. X. 2006, A&A, 448, 955
Jones, A., Noll, S., Kausch, W., Szyszka, C., & Kimeswenger, S. 2013, A&A, 560, A91
Kewley, L. J., Dopita, M. A., Leitherer, C., et al. 2013, ApJ, 774, 100
Kewley, L. J., & Ellison, S. L. 2008, ApJ, 681, 1183
Knop, R. A., Armus, L., Larkin, J. E., et al. 1996, AJ, 112, 81
Komossa, S., & Schulz, H. 1997, A&A, 323, 31
Koratkar, A., & Blaes, O. 1999, PASP, 111, 1
Lilly, S. J., Carollo, C. M., Pipino, A., Renzini, A., & Peng, Y. 2013, ApJ, 772, 119
Lu, K.-X., Zhao, Y., Bai, J.-M., & Fan, X.-L. 2019, MNRAS, 483, 1722
Lu, Y., Blanc, G. A., & Benson, A. 2015, ApJ, 808, 129
Maier, C., Lilly, S. J., Ziegler, B. L., et al. 2014, ApJ, 792, 3
Maiolino, R., & Mannucci, F. 2019, A&ARv, 27, 3
Malkan, M. A., Jensen, L. D., Rodriguez, D. R., Spinoglio, L., & Rush, B. 2017, ApJ, 846, 102
Marconi, A., Moorwood, A. F. M., Salvati, M., & Oliva, E. 1994, A&A, 291, 18
Mathews, W. G., & Ferland, G. J. 1987, ApJ, 323, 456
Matsuoka, K., Nagao, T., Maiolino, R., Marconi, A., & Taniguchi, Y. 2009, A&A, 503, 721
Matsuoka, K., Nagao, T., Maiolino, R., Marconi, A., & Taniguchi, Y. 2011a, A&A, 532, L10
Matsuoka, K., Nagao, T., Marconi, A., et al. 2018, A&A, 616, L4
Matsuoka, K., Nagao, T., Marconi, A., Maiolino, R., & Taniguchi, Y. 2011b, A&A, 527, A100
Morais, S. G., Humphrey, A., Villar-Martín, M., et al. 2017, MNRAS, 465, 2698
Mullaney, J. R., Alexander, D. M., Fine, S., et al. 2013, MNRAS, 433, 622
Nagao, T., Maiolino, R., & Marconi, A. 2006a, A&A, 459, 85
Nagao, T., Maiolino, R., & Marconi, A. 2006b, A&A, 447, 863
Nagao, T., Marconi, A., & Maiolino, R. 2006c, A&A, 447, 157

Nagao, T., Murayama, T., Shioya, Y., & Taniguchi, Y. 2003, AJ, 125, 1729
Nagao, T., Murayama, T., & Taniguchi, Y. 2001a, ApJ, 549, 155
Nagao, T., Murayama, T., & Taniguchi, Y. 2001b, PASJ, 53, 629
Nakajima, K., Fletcher, T., Ellis, R. S., Robertson, B. E., & Iwata, I. 2018, MNRAS, 477, 2098
Nesvadba, N. P. H., De Breuck, C., Lehnert, M. D., Best, P. N., & Collet, C. 2017, A&A, 599, A123
Newman, S. F., Buschkamp, P., Genzel, R., et al. 2014, ApJ, 781, 21
Noll, S., Kausch, W., Barden, M., et al. 2012, A&A, 543, A92
Oke, J. B., Cohen, J. G., Carr, M., et al. 1995, PASP, 107, 375
Oke, J. B., & Gunn, J. E. 1982, PASP, 94, 586
Richards, G. T., Lacy, M., Storrie-Lombardi, L. J., et al. 2006, ApJS, 166, 470
Robinson, A., Binette, L., Fosbury, R. A. E., & Tadhunter, C. N. 1987, MNRAS, 227, 97
Rose, M., Elvis, M., & Tadhunter, C. N. 2015, MNRAS, 448, 2900
Rottgering, H. J. A., Miley, G. K., Chambers, K. C., & Macchetto, F. 1995, A&AS, 114, 51
Sanders, R. L., Shapley, A. E., Reddy, N. A., et al. 2020, MNRAS, 491, 1427
Schlegel, D. J., Finkbeiner, D. P., & Davis, M. 1998, ApJ, 500, 525
Seymour, N., Stern, D., De Breuck, C., et al. 2007, ApJS, 171, 353
Shih, H.-Y., Stockton, A., & Kewley, L. 2013, ApJ, 772, 138
Silva, M., Humphrey, A., Lagos, P., et al. 2018, MNRAS, 474, 3649
Simpson, C., Eisenhardt, P., Armus, L., et al. 1999, ApJ, 525, 659
Solórzano-Iñarrea, C., Best, P. N., Röttgering, H. J. A., & Cimatti, A. 2004, MNRAS, 351, 997
Tadhunter, C. N., Villar-Martin, M., Morganti, R., Bland-Hawthorn, J., & Axon, D. 2000, MNRAS, 314, 849
Terao, K., Nagao, T., Hashimoto, T., et al. 2016, ApJ, 833, 190
Thomas, A. D., Groves, B. A., Sutherland, R. S., et al. 2016, ApJ, 833, 266
Tody, D. 1986, Proc. SPIE, 627, 733
Tody, D. 1993, in ASP Conf. Ser. 52, Astronomical Data Analysis Software and Systems II, ed. R. J. Hanisch, R. J. V. Brissenden, & J. Barnes (San Francisco, CA: ASP), 173
Tremonti, C. A., Heckman, T. M., Kauffmann, G., et al. 2004, ApJ, 613, 898
van Dokkum, P. G. 2001, PASP, 113, 1420
Vangioni, E., Dvorkin, I., Olive, K. A., et al. 2018, MNRAS, 477, 56
Vaona, L., Ciroi, S., Di Mille, F., et al. 2012, MNRAS, 427, 1266
Veilleux, S. 1991, ApJ, 369, 331
Vernet, J., Fosbury, R. A. E., Villar-Martín, M., et al. 2001, A&A, 366, 7
Villar-Martín, M., Fosbury, R. A. E., Binette, L., Tadhunter, C. N., & Rocca-Volmerange, B. 1999, A&A, 351, 47
Villar-Martín, M., Humphrey, A., De Breuck, C., et al. 2007, MNRAS, 375, 1299
White, R. L., & Becker, R. H. 1992, ApJS, 79, 331
Yabe, K., Ohta, K., Iwamuro, F., et al. 2012, PASJ, 64, 60
Yuan, T.-T., Kewley, L. J., & Richard, J. 2013, ApJ, 763, 9
Zheng, W. 1988, ApL&C, 27, 275
Zheng, W., Kriss, G. A., Telfer, R. C., Grimes, J. P., & Davidsen, A. F. 1997, ApJ, 475, 469